Improved Estimation of Temporal Dynamics in the ASCAT Backscatter-Incidence Angle Relation Using Regularization

Frantzen, Paco; Steele-Dunne, Susan; Quaife, Tristan; Vreugdenhil, Mariette; Hahn, Sebastian; Wagner, Wolfgang

DOI
10.1109/JSTARS.2025.3572306

Publication date
2025

Document Version
Final published version

Published in
IEEE Journal of Selected Topics in Applied Earth Observations and Remote Sensing

Improved Estimation of Temporal Dynamics in the ASCAT Backscatter-Incidence Angle Relation Using Regularization

Paco Frantzen, Susan Steele-Dunne, Tristan Quaife, Mariette Vreugdenhil, Sebastian Hahn, and Wolfgang Wagner, *Senior Member, IEEE*

***Abstract*—The relation between microwave backscatter and incidence angle estimated from observations of the Advanced Scatterometer (ASCAT) onboard the Metop satellites contains valuable information on the dynamics of vegetation water content and structure. The relation between backscatter and incidence angle (parameterized using so-called slope and curvature parameter) has been related to vegetation water dynamics in studies on the North American Grasslands and the Cerrado Savannah. The current approach to estimate time series of the slope and curvature parameters involves a kernel smoother, weighing observations according to their temporal distance to the day of interest. While this approach provides a robust representation of backscatter-incidence angle relation over longer time scales, it does not accurately capture the timing of short-term changes. To further improve the correspondence between backscatter-incidence angle relation and vegetation water dynamics, the timing of short-term changes should be preserved in the estimation of slope and curvature. This would allow slope and curvature to be reconciled with independent estimates of biogeophysical variables, and allow us to isolate high-frequency variations due to, for example, intercepted precipitation or soil moisture. Here, an alternative method is introduced to estimate the ASCAT backscatter-incidence angle relation using temporally constrained least squares. While the proposed method yields similar performance to the kernel smoother in aggregated statistics, this method retains the timing of short-term changes.**

***Index Terms*—Microwave Remote Sensing, Radar, Vegetation, Vegetation Water Dynamics, Biomass, Soil Moisture.**

The work of P. Frantzen and S. Steele-Dunne was supported by NWO grant ENW.GO.001.034 as part of the "Use of space infrastructure for Earth observation and planetary research" research program. The work of T. Quaife was supported by the UKRI NCEO International Programme (NE/X006328/1). The work of M. Vreugdenhil, S. Hahn, and W. Wagner was supported by EUMETSAT's Support to Operational Hydrology and Water Management Satellite Application Facility (H SAF). (Corresponding author: P. Frantzen)

P. Frantzen and S. Steele-Dunne are with the Department of Geoscience and Remote Sensing, Delft University of Technology (TU Delft), 2628CN Delft, The Netherlands (e-mail: p.frantzen@tudelft.nl; s.c.steele-Dunne@tudelft.nl). T. Quaife is with the UKRI National Centre for Earth Observation and Department of Meteorology, University of Reading, RG6 6BU Reading, U.K (email: t.l.quaife@reading.ac.uk). M. Vreugdenhil, S. Hahn, and W. Wagner are with the Department of Geodesy and Geoinformation, Vienna University of Technology (TU Wien), 1040 Vienna, Austria (e-mail: mariette.vreugdenhil@geo.tuwien.ac.at; sebastian.hahn@geo.tuwien.ac.at; wolfgang.wagner@geo.tuwien.ac.at).

I. Introduction

RADAR backscattering coefficient (σ°) measurements from the Advanced Scatterometer (ASCAT) instrument onboard the Metop satellites have been used to provide estimates of surface soil moisture since 2007 [1]. Two key parameters in the retrieval of surface soil moisture from ASCAT σ° are the so-called slope (σ') and curvature (σ''), the first and second derivative of the relation between σ° and incidence angle (θ). The role of these parameters in soil moisture retrieval is two-fold. σ' and σ'' are used to normalize σ° measured at different incidence angles (θ) to the reference angle

(θ_{ref}). Additionally, the seasonal variation of the σ' and σ'' are used to account for the influence of the yearly vegetation growth cycle on ASCATs sensitivity to soil moisture [2].

The first use of σ' and σ'', was in the retrieval of soil moisture from SCAT onboard the ERS satellite, in which the yearly cycle of both parameters was modeled through trigonometric functions [2]. To provide an estimate with higher temporal resolution, [3] proposed a method similar to Monte Carlo simulation in combination with a cubic spline to estimate the yearly cycle of σ' and σ''. A computationally less expensive method for the estimation of ASCAT σ' and σ'' yearly cycle was presented in [4], making use of an Epanechnikov kernel smoother. For the retrieval of soil moisture from ASCAT, the Epanechnikov kernel method [4] is currently used to compute a yearly repeating cycle of σ' and σ'' as a function of day of year (discarding interannual variability) based on the full ASCAT data record. Melzer [4] also used the kernel smoother method for dynamic characterization of σ' and σ'', in which the parameters are estimated as a multi-year time series with a value for each date (allowing interannual variability) instead of one for each day of the year. In this approach, for each day a weighted least squares estimation is performed using observations within 21 days from the day of interest, with weights applied to observations as a function of their temporal distance to the day of interest, according to the Epanechnikov kernel.

The use of the backscatter-incidence angle relation as a potential source of vegetation phenology information was first recognized by Wagner et al. [5]. With the dynamic characterization of the σ-θ relation using the method presented in [4], various studies were conducted to use σ-θ relation as a means to investigate vegetation. Global time series of dynamic σ' and σ'' computed using the kernel smoother method were investigated in [6]. Vegetation optical depth was estimated from ASCAT using the σ-θ relation, and its use for vegetation monitoring was demonstrated by Vreugdenhil et al. [7]. The σ-θ relation was utilized to investigate vegetation response to drought in the North American grasslands [8] and the Cerrado Savannah [9]. Phenological observations were linked to changes in σ-θ relation by Pfeil et al. [10] to investigate ASCATs sensitivity to spring reactivation in broadleaf forests. The relation between land surface model variables and the σ-θ relation were investigated using a deep neural network by Shan et al. [11]. Although the σ-θ relation could be used in studies of vegetation at longer time scales and in aggregated statistics, Greimeister-Pfeil et al. [12] found that high-frequency variation of dynamic σ' is partially caused by soil moisture and recommended further investigation of the soil moisture influence on dynamic σ' and mitigation methods.

An important step to advance the exploitation of the σ-θ relation for monitoring of vegetation is to understand the factors driving short-term variation in the σ-θ relation. However, the current estimation of the σ-θ relation using the Epanechnikov kernel smooths out short-term features [13], obstructing the ability to disentangle short-term variation from the seasonal cycle. Thus, to investigate the influence of short-time-scale processes on the σ-θ relation, a smoothing kernel should be avoided in the estimation of the σ' and σ'' parameters.

In this study, we investigate the use of temporally constrained least squares estimation, proposed by Quaife in [14] as an alternative method to estimate the σ-θ relation without the adverse artifacts of a smoothing kernel at short time scales. This method is based on the constrained inversion by Twomey [15], and is also referred to as Tikhonov Regularization. To provide robust estimates of σ' and σ'' using this method, a constraint is applied to the first differences following [14]. We compare the ability of the current and novel method to capture changes in the input data at short time scales using observations from ASCAT as well as simple input signals simulating isolated events. The methods are also evaluated by using the σ-θ relation estimates from Metop-A, to estimate so-called "local slopes" observed by Metop-B, and comparing those to the observations.

II. Data and Methods

A. ASCAT

ASCAT is the scatterometer onboard the Metop satellites, observing σ° at near-daily intervals for most locations on Earth since 2007. ASCAT data used in this study are sampled on an earth-fixed Fibonacci grid with a 6.25 kilometer sampling distance [16]. For a grid point, ASCAT measures backscatter σ° using its fore (f), mid (m), and aft (a) antenna per overpass. Due to the orientation of the antennas, the incidence angle θ from which σ° is measured, differs for the three σ° measurements, with $\theta_f \approx \theta_a$ and θ_m being lower. The actual values of θ for each beam vary for different overpasses due to changes in viewing geometry. The variation in observed incidence angles allows the relation between σ° and θ to be estimated. This relation is represented by two parameters, σ' and σ'', the parameters of a second order Taylor polynomial assumed to describe σ° as a function of θ around a reference angle θ_{ref} according to Equation 1:

$$\sigma^\circ(\theta) = \sigma^\circ(\theta_{ref}) + \sigma'(\theta - \theta_{ref}) + \sigma''(\theta - \theta_{ref})^2 \tag{1}$$

In this equation, $\sigma^\circ(\theta)$ is the backscattering coefficient at incidence angle θ, σ' is the linear term of the Taylor polynomial, referred to as the slope, and σ'' is the quadratic term or curvature. This model of the backscatter-incidence angle relation allows the normalization of backscatter coefficients observed at multiple angles to a single reference angle (generaly defined to be 40). In addition, dynamics of σ' and σ'' can be used to study vegetation due to their sensitivity to vegetation water content and structure and limited sensitivity to fluctuations in surface reflectivity. In the remainder of this section, the steps required in the estimation of σ' and σ'' from ASCAT observations are discussed.

Three near-simultaneous backscatter measurements (σ_m^{circ}, σ_f^{circ} and σ_a^{circ}, where the subscripts indicate measurements from the mid-, fore- and aft-beams) and their respective θ per overpass of ASCAT allow an instantaneous linear approximation of the relation between σ° and θ. First using Equation 2, two linear approximations, $\sigma'_{m,f}$ and $\sigma'_{m,a}$ are computed using σ° from two different combinations of beams.

$$\sigma'_{m,f/m,a} = \frac{\sigma^\circ_m - \sigma^\circ_{f/a}}{\theta_m - \theta_{f/a}} \tag{2}$$

Next, the mean of $\sigma'_{m,f}$ and $\sigma'_{m,a}$ is computed, resulting in one so-called local slope (σ'_{loc}) for each overpass:

$$\sigma'_{loc} = \frac{\sigma'_{m,f} + \sigma'_{m,a}}{2} \tag{3}$$

Since the σ'_{loc} is a linear approximation, and the relation between θ and σ° is assumed to be quadratic, σ'_{loc} is only valid at a corresponding θ_{loc}, which is computed using a weighed mean of θ_f, θ_a and θ_m. The σ' and σ'', can be estimated with multiple values of σ'_{loc} and θ_{loc} using:

$$\sigma'_{loc}(\theta) = \sigma' + \sigma''(\theta_{loc} - \theta_{ref}) \tag{4}$$

Many σ'_{loc} values are needed to estimate the σ°-θ relation, to ensure that measurements are available at a variety of θ_{loc}, and because these individual measurements are noisy.

B. ASCAT σ' and σ'' using Epanechnikov kernel

In the current kernel smoothing approach, time series of dynamic σ' and σ'' are estimated using an Epanechnikov kernel as proposed in [4] and further studied in [6].

To estimate the σ' and σ'' for a day d_0, weights are assigned to the σ'_{loc} in the period around d_0 as a function of their temporal distance to d_0, following the shape of the Epanechnikov kernel. The weight assigned to a σ'_{loc} on day d_i is obtained through Equation 5:

$$w(d_i) = \begin{cases} \frac{3}{4}\left(1 - (d_i - d_0)^2\right), & \text{if } |d_i - d_0| \leq hw \\ 0, & \text{otherwise} \end{cases} \tag{5}$$

In this equation, $w(d_i)$ is the weight assigned to the observation on day d_i, and *hw* is the half-width of the epanechnikov kernel. Next, the σ' and σ'' on day d_0: $\begin{bmatrix}\sigma'_{d0} & \sigma''_{d0}\end{bmatrix}$ are obtained through the weighted least squares estimation using the relation presented

in Equation 4 along with the weights corresponding to the σ'_{loc} from Equation 5:

$$\begin{bmatrix}\sigma'_{d_0} & \sigma''_{d_0}\end{bmatrix} = (\mathbf{A}^T\mathbf{W}_{d_0}\mathbf{A})^{-1}\mathbf{A}^T\mathbf{W}_{d_0}\mathbf{y} \quad (6)$$

$\mathbf{y}$ is the observation vector, containing all σ'_{loc} observed within *hw* days from d_0, $\mathbf{W}_{d_0}$ is a matrix containing the weights $w(d_i)$ of the respective σ'_{loc} as determined through Equation 5, and $\mathbf{A}$ is the design matrix implementing the relation Equation 4 through a column of ones and a column of $(\theta_{loc} - \theta_{ref})$ values. The computation of weights and weighted least squares estimation are repeated for each day in the considered period to obtain a time series of σ' and σ''. The full parameterization of the σ°-θ relation (consisting of normalized σ°, σ' and σ'') using this kernel smoothing method is denoted as E and time series of σ' obtained using this method will be referred to as σ'_E. Different half-widths are considered in this study to investigate its influence on σ'_E.

C. Proposed approach using regularization

An alternative method for the estimation of dynamic σ' and σ'' from ASCAT data is an implementation of the method for temporally constrained least squares estimation proposed by Quaife [14] based on methods by Twomey [15]. In this approach, a constraint is applied to the first differences in the estimated time series. The entire time series of σ' and σ'' are estimated in a single calculation, using all available σ'_{loc} and corresponding θ_{loc}. If uniform weights are applied to the individual observations, the equation to obtain the estimated time series $\hat{\mathbf{x}}$ using the method for temporally constrained least squares is:

$$\hat{\mathbf{x}} = (\mathbf{A}^T\mathbf{A} + \gamma^2\mathbf{B}^T\mathbf{B})^{-1}\mathbf{A}^T\mathbf{y} \quad (7)$$

where $\hat{\mathbf{x}}$ is a vector containing augmented time series of the estimated parameters, $\mathbf{A}$ is the design matrix linking $\hat{\mathbf{x}}$ to the vector of observations $\mathbf{y}$, and $\mathbf{B}$ is a first difference matrix corresponding to the size of $\hat{\mathbf{x}}$. The scalar γ, which is multiplied with $\mathbf{B}$ is a Lagrangian multiplier, driving the influence of the first difference constraint on the estimated time series in $\hat{\mathbf{x}}$, with larger values of γ corresponding to a stronger constraint on the first differences. For the trivial case of $\gamma = 0$, the ordinary least squares estimation is obtained, while for $\gamma \to \infty$, the estimated time series in $\hat{\mathbf{x}}$ approaches a constant value for each parameter.

To estimate the time series of σ' and σ'' using this method, $\hat{\mathbf{x}}$ is a $2n$ length vector containing n estimated σ' values and n values of σ'' respectively, where n corresponds to the number of time steps for which the estimation is performed. In this study, σ' and σ'' are estimated on a daily interval, for the period in which observations from ASCAT aboard Metop-A are available (2007-01-01 to 2021-11-15). $\mathbf{y}$ is the vector of m observations, that are all σ'_{loc} observed by ASCAT aboard Metop-A for the considered period. $\mathbf{A}$ is the design matrix that links the σ'_{loc} observations and the corresponding incidence angles θ to the estimated parameters according to Equation 4. To implement this relation in a matrix linking $\hat{\mathbf{x}}$ and $\mathbf{y}$, the $m \times 2n$ matrix $\mathbf{A}$ contains a 1 at locations $\mathbf{A}[i,j]$ if the epoch of local slope $\mathbf{y}[i]$ occurs on the day corresponding to $\hat{\mathbf{x}}[j]$, and contains the term $(\theta_{loc}[i] - \theta_{ref})$ corresponding to $\mathbf{y}[i]$ at location $\mathbf{A}[i, j+n]$. Assuming one σ'_{loc} is available for each of the n days ($m = n$), $\mathbf{A}$ looks like:

$$\left[\begin{array}{cccc|cccc} 1 & 0 & \dots & 0 & \delta\theta_0 & 0 & \dots & 0 \\ 0 & 1 & \dots & 0 & 0 & \delta\theta_1 & \dots & 0 \\ \vdots & \vdots & \ddots & \vdots & \vdots & \vdots & \ddots & \vdots \\ 0 & 0 & \dots & 1 & 0 & 0 & \dots & \delta\theta_m \end{array}\right]$$

If multiple observations of σ'_{loc} are available on the same date, their corresponding 1 and $\delta\theta_i = (\theta_i - \theta_{ref})$ are placed in the same column as the other observations corresponding to that date. Furthermore, if no observations are available for a specific date, the column in $\mathbf{A}$ corresponding to that date is filled with zeros. The $2n \times 2n$ first difference

matrix $\mathbf{B}$ corresponds to:

$$\begin{bmatrix} 0 & 0 & & & & & \\ -1 & 1 & 0 & & & & \\ 0 & -1 & 1 & 0 & & & \\ & & \ddots & \ddots & \ddots & & \\ & & 0 & -10 & 10 & 0 & \\ & & & 0 & -10 & 10 & \end{bmatrix} \tag{8}$$

A row of zeroes occurs on the first row in $\mathbf{B}$ because no difference can be computed without a preceding day. Row $n+1$ is also filled with zeroes to avoid a constraint on the difference between the last estimate of σ' and the first estimate of σ''. To estimate both σ' and σ'', the final n rows of $\mathbf{B}$ (corresponding to the first differences of σ'') are multiplied by 10. This effectively multiplies γ by 10 for the σ''estimates, and accounts for the difference in magnitude of day-to-day changes between σ' and σ''. Finally, the matrix $\mathbf{B}$ is multiplied by a Lagrangian multiplier γ, driving the influence of the first difference constraint on the estimated time series. In this study, σ' and σ'' time series are estimated for various values of γ to investigate the optimal strength of the constraint. The values of smoothing parameter γ considered in this study are 1, 2, 4, 6, 8, and 10. It will be shown that this range of values results in smoothing effects comparable to the Epanechnikov kernel with a half-width of 11 to 31 days. The full parameterization of the σ°-θ relation using this regularization method are denoted by R and slope time series computed using this method are denoted as σ'_R.

Although both slope and curvature are impacted by a change in their estimation method, results presented in this research focus mainly on the slope parameter because of its expected higher sensitivity to dynamics of vegetation water content compared to curvature [8, 9]. Furthermore, the impact of changing the method for estimating slope and curvature are similar for both parameters. In the cross-validation presented in subsection III-C, performance metrics presented in the results are affected by both slope and curvature, as shown in Equation 9.

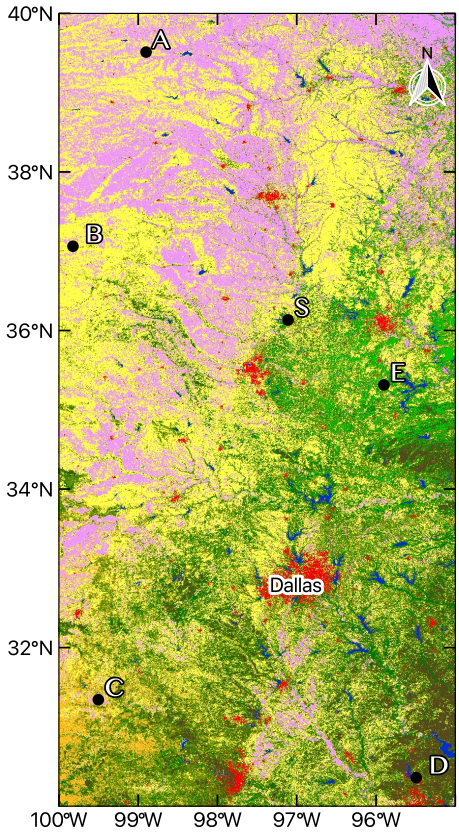

Fig. 1. Copernicus dynamic land cover map of 2015[17], along with an indication of the Dallas urban area and the location of the four example time series shown in Figure 10.

D. Study area

The study area is the region spanning latitudes $30°N$ to $40°N$ and longitudes $100°W$ to $95°W$. This region includes parts of Texas, Oklahoma, and Kansas, and contains a variety of vegetated land covers as shown in Figure 1, and elaborated in Table I.

Land cover data from the Copernicus dynamic land cover map [17] are shown in Figure 1. The color code, abbreviation (Abrv.), class identifier (ID), and short description are given in Table Table I. Data from 2015 are used because it occurs in the middle of the ASCAT data record, which

extends from 2007 to 2022. In subsection III-C, 1492 randomly selected ASCAT grid points within the study area will be used to compare the estimation methods, representing the distribution of land cover types in the area of interest. Initially, 1500 grid points were ramdomly selected to represent roughly 10% of the available grid points in the study area, and 8 were filtered out because urban areas were the dominant land cover in their proximity. The distribution of land cover types for these 1492 points is provided in Figure 2. An offline analysis for a single value of γ was conducted to ensure that the sample of 1492 grid points is representative of the population of all grid points in terms of land cover distribution and performance statistics.

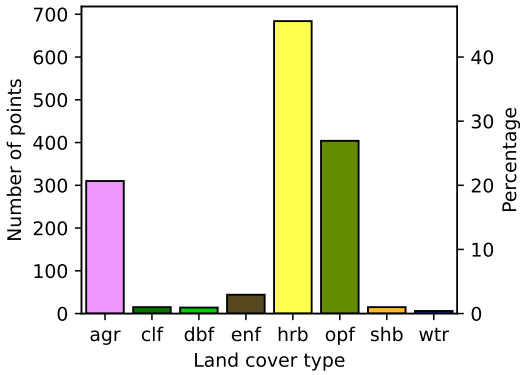

Fig. 2. Distribution of land cover types among the subset of 1492 points within the study area.

Color	Abrv.	ID	Description
	shb	20	Shrubs
	hrb	30	Herbaceous vegetation
	agr	40	Agriculture.
	urb	50	Urban, paved
	wtr	80	Permanent water bodies
	enf	111	Evergreen needle leaf forest
	dbf	114	Deciduous broad leaf forest.
	clf	116	Closed forest
	opf	126	Open forest

TABLE I
COMMON LAND COVER TYPES IN THE STUDY AREA.

E. Qualitative comparison of time series

Two years of σ'_E and σ'_R for a range of *hw* and γ values are compared to investigate the difference between the two estimation methods, including the influence of smoothing. The time series are computed using Metop-A ASCAT observations at the grid point closest to the Stillwater-5-WNW USCRN station [18, 19] (indicated "S" on Figure 1). In-situ soil moisture from the Stillwater station and LAI from MODIS [20] are also plotted to provide insight into soil moisture and vegetation changes. A 14 day moving average is applied over the MODIS LAI data to provide a smoother time series. The qualitative comparison also includes comparisons of temporal derivatives of σ'_E and σ'_R and their lagged correlation to daily changes in soil moisture.

F. Simple change response

The response of the Epanechnikov and constrained least squares method to four simple types of changes in the input signal are considered to understand the occurrence of artifacts in the two different estimation methods. The four considered input signals represent temporal features likely to be encountered in a time series of radar observations over a vegetated land surface. These input signals are defined as a steady state where a certain event occurs on the arbitrary day d. Visual representations of the input signal are provided along the results. The simple impulse is defined as:

$$f_i(d) = \begin{cases} -1, & \text{if } d = 50 \\ 0, & \text{otherwise} \end{cases}$$

This signal is considered to understand the influence of an intermittent impulse, e.g. the occurrence of precipitation or some perturbation to the observation that needs to be isolated from the vegetation term.

The step function is defined as follows:

$$f_s(d) = \begin{cases} -1, & \text{if } d \geq 50 \\ 0, & \text{otherwise} \end{cases}$$

This represents sudden changes that could occur in ASCAT σ' such as a change in the freeze/thaw state, snowfall, or a sudden change in vegetation cover

e.g. due to forest fire or storm damage. The double impulse signal is described as:

$$f_{di}(d) = \begin{cases} -1, & \text{if } d = 38 \text{ or } d = 62 \\ 0, & \text{otherwise} \end{cases}$$

This represents the occurrence of two impulses separated in time by an interval shorter than $2 \times hw$ for σ'_E, or at a time scale where the temporal constraint outweighs the influence from observations for σ'_R. For example, it could be two precipitation events separated by a few weeks.

The final simple signal considered is the exponential decay, defined as:

$$f_e(d) = \begin{cases} -e^{\frac{d-50}{5}}, & \text{if } d \geq 50 \\ 0, & \text{otherwise} \end{cases}$$

This signal simulates the influence of soil moisture changes in response to precipitation. The sudden increase in soil moisture due to the precipitation event is followed by an exponential decline as the soil dries down.

G. Cross-validation using Metop-B

Observations from ASCAT onboard Metop-A are used to estimate time series of σ' and σ'' in this study. The temporal overlap of Metop-B with Metop-A (2013 to 2022) allows us to use Metop-B data as cross-validation data. Hahn et al. [6] estimated σ' and σ'' from Metop-A and Metop-B separately and argued that the consistency between the two products demonstrated the robustness of the kernel smoothing approach. Here, the comparison is not in terms of σ' and σ'', but in terms of σ'_{loc}. In particular, the σ' and σ'' estimated from Metop-A are combined with the incidence angles from Metop-B to estimate the local slopes of Metop-B ($\hat{\sigma}'_{loc}$), these estimated local slopes can then be compared to the real σ'_{loc} observed by Metop-B to assess the performance of the σ°-θ relation estimation methods. We do not compare σ' and σ'' from Metop-A to σ' and σ'' from Metop-B because we want to assess how well the dynamics of estimated σ°-θ relation time series correspond to dynamics of the real σ°-θ relation, which varies at daily time scales. σ' and σ'' (as oppossed to σ'_{loc}) from Metop-B do not reflect the dynamics of the σ°-θ relation observed by Metop-B because σ' and σ'' are temporally aggregated estimated parameters, while local slopes are instantaneous representations of the true σ°-θ relation.

To compute the estimated local slopes based on Metop-A σ' and σ'', a time-varying extrapolation is performed according to Equation 9:

$$\hat{\sigma}'_{loc} = \sigma'_A + \sigma''_A(\theta_{loc_B} - \theta_{ref}) \tag{9}$$

In this equation, $\hat{\sigma}'_{loc}$ is the time series of estimated local slopes at the incidence angles θ_{loc_B}. with θ_{loc_B} being the time series of incidence angles corresponding to σ'_{loc_B}. σ'_A and σ''_A are the σ' and σ'' time series estimated using only Metop-A observations. A temporal collocation must be performed because the epochs of σ'_{loc_B} do not occur at noon at a daily interval. It is chosen to link the σ'_{loc_B} observations closest to noon to σ'_A and σ''_A for each day. On days when no σ'_{loc_B} is available, no comparisons are made.

The bias, unbiased root mean squared error (ubRMSE), and Pearson correlation coefficient between observed (σ'_{loc_B}) and estimated ($\hat{\sigma}'_{loc}$) local slopes from Metop-B for each grid point are calculated to compare the performance of the two methods for estimating the σ°-θ relation. $\hat{\sigma}'_{loc}$ time series computed using the σ' and σ'' from the Epanechnikov kernel are denoted as $\hat{\sigma}'_{loc_E}$ and those computed using the σ' and σ'' from the regularization method are denoted as $\hat{\sigma}'_{loc_R}$

The three performance metrics are computed for the time series of 1492 random grid points located in the study area as described in subsection II-D. To investigate the influence of γ on σ'_R for different land covers, the three metrics are computed for time series of $\hat{\sigma}'_{loc_R}$ with γ values of 1,2,4,6,8, and 10, and averaged for each land cover. Violin plots of the metrics for $\hat{\sigma}'_{loc_R}$ with $\gamma = 6$ and $\hat{\sigma}'_{loc_E}$ with $hw =$ 21 days are created to compare the performance of both estimation methods for different land covers. The ubRMSE and bias averaged over all 1492 points are computed to compare the performance of σ'_E and σ'_R under varying smoothing constraints, varying hw and γ, respectively. Finally, the three performance metrics are mapped to compare spatial

patterns in the performance of the Epanechnikov and regularization method.

III. RESULTS

A. Artefacts in ASCAT daily σ' estimates

Slope time series estimated using observations from ASCAT aboard Metop-A are shown in Figure 3, along with soil moisture and LAI at the same location. From Figure 3(a), it is clear that LAI has a strong seasonal cycle, while soil moisture varies in response to precipitation events at intervals from days to weeks. Both σ'_E and σ'_R exhibit a seasonal cycle. However, this seasonal cycle does not follow LAI exactly due to the sensitivity of microwave observations to both vegetation water content and structure.

The σ'_R computed using the proposed regularization method is shown in Figure 3(b) while the σ'_E, calculated using the current smoothing kernel method is shown in (c). Figure 3(c) shows σ'_E estimated with various half-widths. The yearly cycle is similar for all half-widths, but the amplitude of short-term fluctuations is larger for lower half-widths. In addition, the timing of short-term fluctuations varies depending on half-width. So, increasing *hw* leads to a smoother estimate of σ'_E, but introduces artifacts in the estimated time series due to short-term fluctuations in the observations.

In Figure 3(b), σ'_R estimated with various values of γ are shown. The amplitude of short-term fluctuations is larger for lower values of γ. Therefore, increasing γ leads to a smoother estimate of σ'_R. While all σ'_R time series follow the same yearly cycle as those of σ'_E, differences are clear at shorter time scales. In particular, σ'_E is generally smoother than σ'_R. More importantly, the timing of high-frequency oscillations is consistent across σ'_R estimates regardless of γ while these are lost or displaced in time in the σ'_E estimates. The differences between σ''estimated using the Epanechnikov and regularization method (presented in Figure 15) are consistent with the discussed differences between σ'_R and σ'_E.

Figure 4 (a) and (b) highlight the difference between estimated σ'_R and σ'_E around a precipitation event in October 2010, and how the impact of soil moisture on the estimated slope varies with γ and half-width respectively. Figure 4(c) shows how the σ°-θ relation varies before and after the soil moisture increase for both methods (R and E). This relationship is modelled using σ' and σ'', and normalized σ° (at the reference incidence angle $\theta = 40°$), obtained by interpolating the σ° measured from the fore, mid and aft antenna at the respective day to the reference angle using σ' and σ'', and computing their mean. Figure 4(c) demonstrates the impact that the difference in slope and curvature estimated using the two techniques translate to a difference in the σ°-θ relation.

At t_0, the soil is relatively dry. The values of σ'_R and σ'_E in Figure 4(a) and (b) do not differ much at this epoch. This is reflected in the correspondence between R and E at t_0 in Figure 4(c), where discrepancies between R and E are small, and largely result from a more curved relation in E . The observed σ° fairly agrees with the modelled relation. Precipitation events between t_0 and t_1 increase surface soil moisture at t_1. The values of σ'_R and σ'_E in Figure 4(a) and (b) respectively, all decrease at different magnitudes from t_0 to t_1. The changes in σ'_E with 21 and 31 day *hw* are small compared to changes in other σ' time series. In Figure 4(c) The difference between R (γ=6) and E (*hw*=11 days) during wet conditions is apparent. Not only is the slope slightly steeper for the regularization method at t_1, but at the reference incidence angle, the contrast between σ° at dry (t_0) and wet (t_1) conditions is higher for R than for E. The regularization method yields higher modelled σ° at very high incidence angles, suggesting a lower sensitivity to soil moisture fluctuations at these incidence angles. The observed σ° of the fore and aft antenna t_1 near $\theta = 60°$ are nearly identical. The three σ° measurements at this epoch correspond better to the steeper relation represented in R than that of E. All values of σ'_R have increased in the drying period between t_1 and t_2 in Figure 4(a), whereas in (b) only the σ'_E with 11 days *hw* has increased, and the σ'_E with longer *hw* have again decreased slightly, resulting in similar σ'_E and σ'_R at t_2. The difference between R (γ=6) and E (*hw*=11 days) in Figure 4(c) is small around the reference

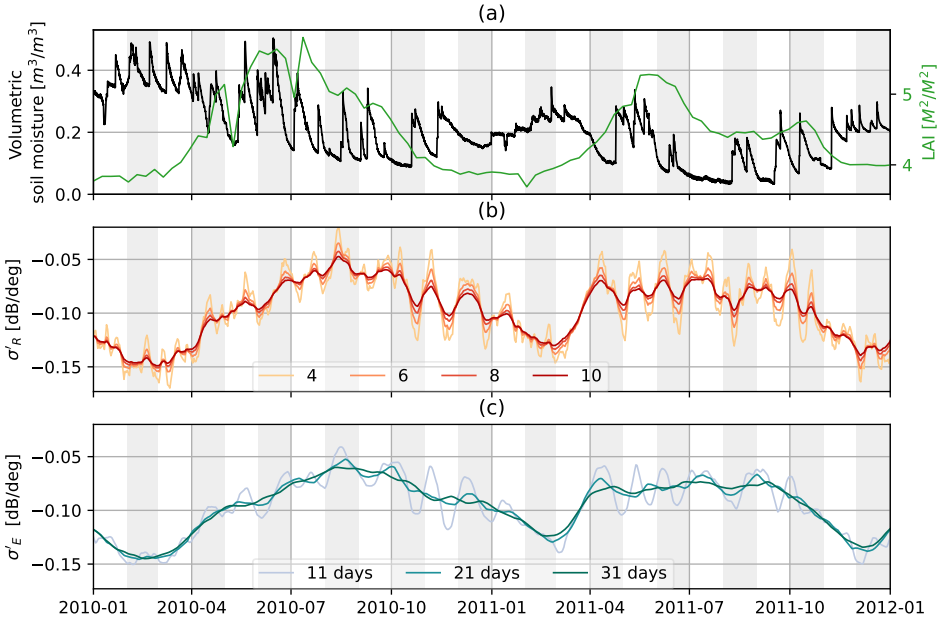

Fig. 3. Two years of ASCAT slope time series near Stillwater, Oklahoma, USA. The top panel (a) shows in-situ soil moisture observations from the Stillwater-5-WNW station[18] and leaf area index (LAI) from MODIS[20]. The middle panel (b) shows σ'_R with γ values of 4, 6, 8, and 10. (c) shows σ'_E with kernel half widths of 11, 21, and 31 days.

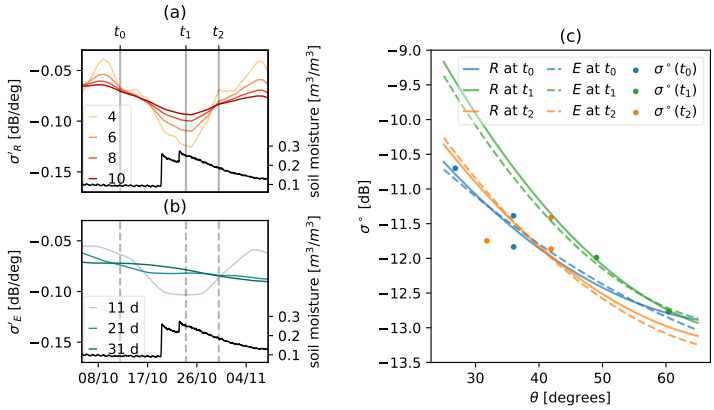

Fig. 4. 34 days of ASCAT slope time series near Stillwater, Oklahoma, USA around a precipitation event. (a) and (b) show σ'_R and σ'_E, respectively, corresponding to Figure 3. In-situ soil moisture observations from the Stillwater-5-WNW station[18] are included in (a) and (b). t0, t1, and t2 define three different dates around the precipitation event. The right panel (c) shows the relation between σ° and θ as modelled using the regularization method R ($\gamma = 6$) and the smoothing kernel method E (11 days hw), as well as σ° observed by the three individual antennas of ASCAT on dates t_0 (2010-10-12), t_1 (2010-10-24) and t_2 (2010-10-30).

angle of 40, and increases towards higher incidence angles. The σ° correspond to neither R nor E at t_2.

B. Responses to simple changes

The difference in response of σ'_E and σ'_R to the simple changes in the input signal is illustrated

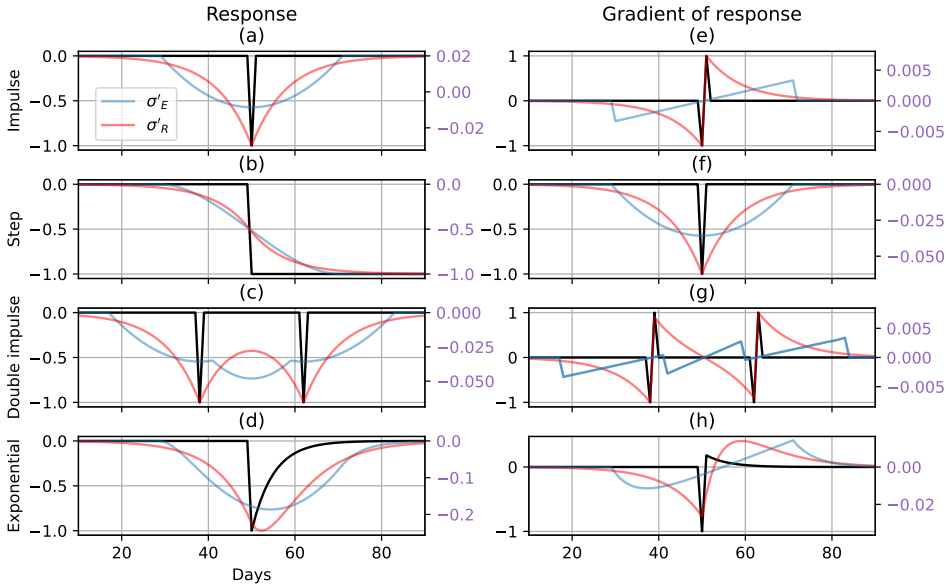

Fig. 5. Response of Epanechnikov kernel (blue) and regularization method (red) to an impulse shown in black: single impulse (a), step (b), double impulse (c) functions, and a step followed by an exponential decay (d). The left shows the signal and response and the right column shows the corresponding temporal derivatives (e)-(h). The regularization response is computed with $\gamma = 8$, the Epanechnikov response is computed with a 21 day *hw*. Purple axes correspond to the values of the regularization and Epanechnikov responses. Black axes denote the values of the input functions.

in Figure 5. Firstly, the influence of the weight distribution in σ'_E is to dampen any peak and spread its influence in time, so that there is no clear dip in σ'_E when the impulse actually occurs. Furthermore, when two impulses occur in quick succession, the superposition of the two responses leads to a local maximum between the two dips (Figure 5(c)). Due to this superposition effect, σ'_E does not capture the timing of an impulse, since the local minimum in the signal may be the result of one or multiple events within a kernel length. The influence of the pulse is also distributed in time by the σ'_R. However, it preserves the timing of the impulse.

The influence on the temporal derivative is also interesting. For all simple change signals except the step change (in Figure 5(e), (g), and (h)), the temporal derivative of σ'_E is low or minimal around the impulse, and at a maximum magnitude at one kernel half-width from the impulse. In contrast, the largest changes in the temporal gradient occur during the impulse itself.

In general, a change in input signal influences the estimated time series for a longer period in σ'_R compared to σ'_E because the entire series is used to obtain the estimate. However, the impact on the estimate occurs at the time of the change, preserving temporal variability. Therefore, short-term changes in observations are better captured around the actual epoch where the change occurs in the σ'_R compared to σ'_E.

Figure 6(a) compares σ'_E with 21 days and σ'_R with γ = 6, highlighting the difference in timing of short-term fluctuations between the two estimates. For example, in July 2010 local minima of σ'_E occur around local maxima of σ'_R and vice versa. Between October 2010 and January 2011, fluctuations occur in the σ'_R where a steady decrease occurs in σ'_E. The temporal derivative of both slope time series in Figure 6(b) highlights the difference in the timing of peaks and sudden changes in σ'_E and σ'_R. In

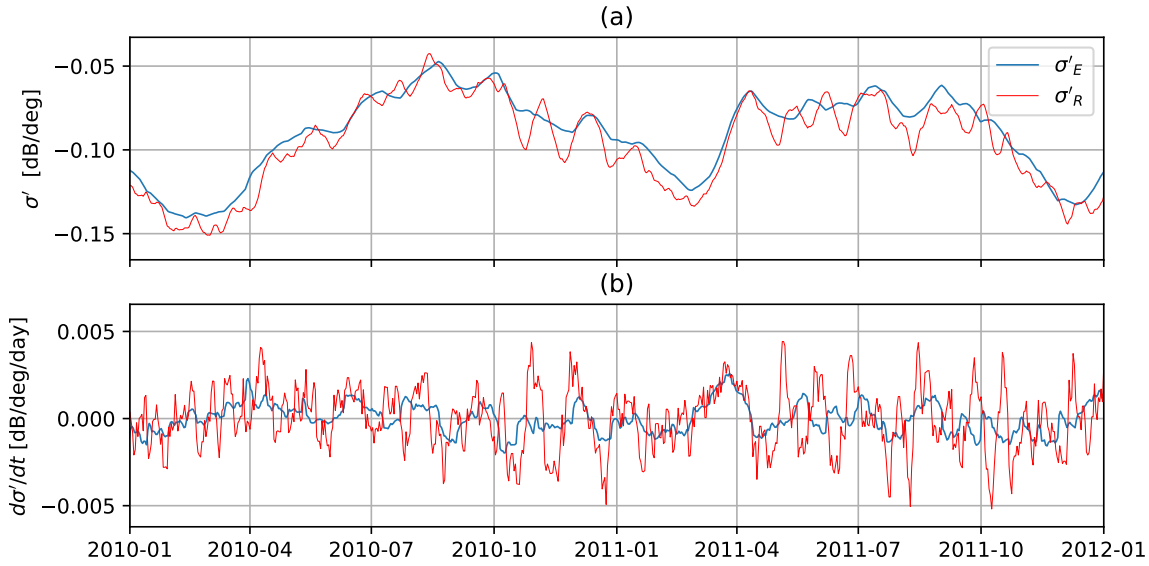

Fig. 6. Two years of ASCAT slope time series (a) and their temporal derivative (b) near Stillwater, Oklahoma, USA. Time series are estimated using the Epanechnikov kernel (σ'_E) with 21-day half-width, and the regularization method (σ'_R) with $\gamma = 6$.

July 2010, the temporal derivatives of σ'_E and σ'_R have opposite signs during the whole month. The derivative of σ'_R fluctuates with larger amplitude, and at shorter periods than that of σ'_E. This difference is in line with the behavior seen Figure 5, where the temporal derivative of the Epanechnikov response is smoother than that of the regularization response, and the timing of changes is represented better in the regularization response. This indicates that differences in the response in Figure 5 between the two methods are also apparent in the real-time series of σ' estimated using the respective methods. In particular, the analogy with Figure 5(h) suggests that in areas where ASCAT σ' is partially driven by variation in surface soil moisture[12], strong dips in the temporal gradient of σ'_R could be indicative of precipitation events and the subsequent dry-down period.

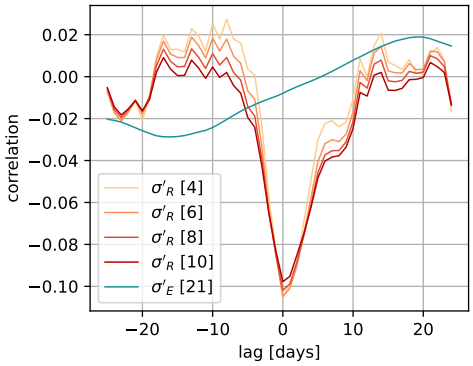

Fig. 7. Pearson correlation coefficient between the temporal derivatives of in-situ soil moisture and estimated σ' for a range of lags between the soil moisture and slope time series. Positive lag corresponds to a delay of soil moisture.

Figure 7 shows the correlation of Stillwater in-situ soil moisture changes with the temporal derivatives of σ'_E at 21-day half-width and σ'_R for various values of γ. First, note that the correlation is generally small because the slope is primarily driven by vegetation. For σ'_E with a half-width of 21, the correlation varies between -0.03 and +0.02. The correlation between soil moisture changes and

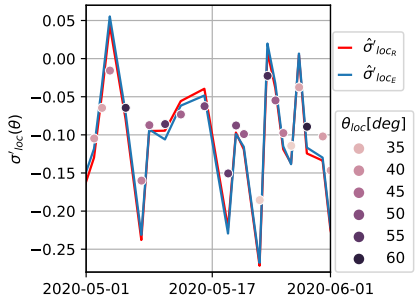

Fig. 8. σ'_{loc_B} (dots) of one grid point, coloured by θ_{loc}, together with $\hat{\sigma}'_{loc}$ estimated using the regularization method ($\hat{\sigma}'_{loc_R}$) with γ of 6, and the smoothing kernel method ($\hat{\sigma}'_{loc_E}$) with a 21 day *hw*.

σ'_R is also close to zero beyond a lag of +/- 10 days. However, there is a relatively larger negative correlation when the lag is close to zero. This shows that there is a link between soil-moisture fluctuations and σ'_R short-term variability, and also highlights the importance of capturing the timing of σ' changes when a comparison is made to time series of geophysical variables subject to short-term fluctuations, such as in [12].

C. Cross validation using Metop B local slopes

Figure 8 illustrates how the local slopes observed by Metop-B can be used as validation data to assess the performance of the two approaches. The observations σ'_{loc_B} are illustrated as filled circles, colored by incidence angles, and shown in Figure 8. The estimated local slopes ($\hat{\sigma}'_{loc_E}$ and $\hat{\sigma}'_{loc_R}$) are obtained using σ'_E and σ'_R from Metop-A together with Equation 9. The $\hat{\sigma}'_{loc_E}$ and $\hat{\sigma}'_{loc_R}$ time series estimated from Metop-A correspond well to the local slopes observed by Metop-B at different incidence angles. Though both correspond well to σ'_{loc_B}, there are differences between $\hat{\sigma}'_{loc_E}$ and $\hat{\sigma}'_{loc_R}$ due to differences in the σ°-θ relation estimation methods used to compute the estimated local slopes.

In the following paragraphs, the performance metrics for this validation in terms of Metop-B local slope will be presented for the whole domain. First, it is important to highlight that the temporal characteristics of σ' (and σ'') vary per cover type, which influences the statistics. The mean and range of slope in the study area are mapped in Figure 9. Slope mean and range vary throughout the area that is used for validation of the slope estimation methods. Low σ' values occur in the croplands and grasslands of the northwest, whereas high values occur in the forests of the southeast. The σ' range follows a similar pattern, with high values in the northwest due to the large seasonality of vegetation cover in agricultural areas compared to the forested areas in the southeast, where lower ranges of σ' occur. The spatial variation in σ' mean and range ensures that the performance of slope estimation methods is validated for a variety of conditions corresponding to different behavior of σ'.

Figure 10 shows the estimated daily slope time series at five different locations in the study area, corresponding to different land covers. A strong yearly cycle occurs for the crops and shrub land covers, in contrast with the stable slope that occurs at the evergreen needle leaf forest. Timing and magnitude of fluctuations differ between σ'_R and σ'_E in each land cover. For σ'_R, short term fluctuations are present in all land cover types, though their amplitudes vary. The difference in long-term variability between land cover types has an effect on the performance metrics used. Specifically, higher Pearson correlation coefficients are expected for land covers with high amplitude long-term fluctuations such as a seasonal cycle. For land covers with large expected variability of slope and a similar level of noise, an increased signal to noise ratio (SNR) will occur for both the Metop-A and Metop-B observations, which in turn elevates the Pearson correlation coefficient [21].

Figure 11 shows the ubRMSE, correlation coefficient, and bias for different values of gamma, colored by land cover type. First, note that both the ubRMSE and correlation are generally highest for agriculture and herbaceous vegetation and relatively low in forest and shrublands. This is partly because the slope itself has a larger range of values in shorter vegetation. This is clear from Figure 9. In contrast, the range of slope in the forested areas in the southeast of the domain is much lower and the mean slope is higher. In forest vegetation, the

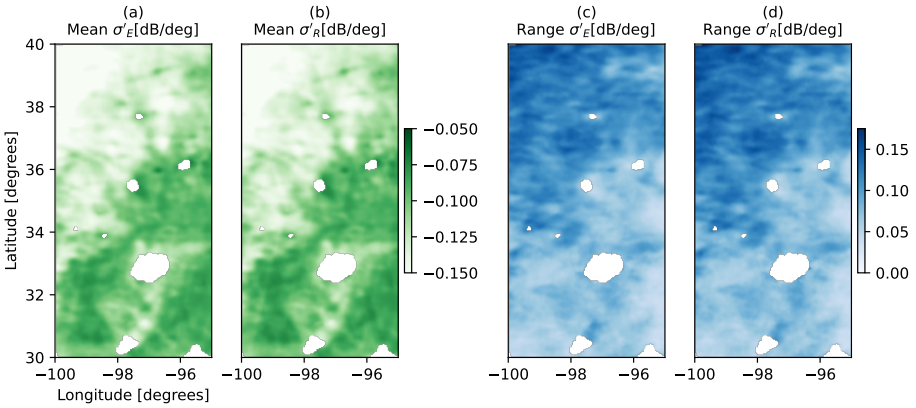

Fig. 9. mean σ'_E (a) and σ'_R (b), and range of σ'_E (c) and σ'_R (d), for Metop-A in the study area, with masked urban areas.

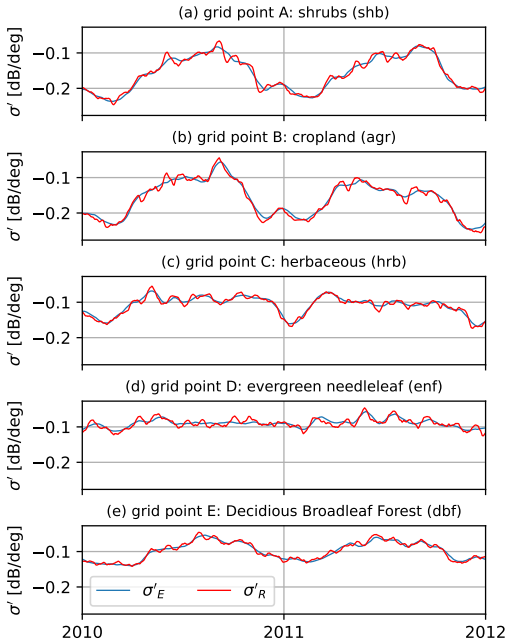

Fig. 10. four σ'_R (γ=6) and σ'_E (half-width=21 days) time series corresponding to different land cover types, for locations indicated on Figure 1.

slope is high and stable. In short vegetation, the slope is lower, varies during the year, and is more likely to be affected by contributions, specifically short-term variations, from the soil surface. In Figure 11(a) the ubRMSE for cropland and herbaceous vegetation is minimum at γ=6 and 8, respectively. For shrublands, the ubRMSE is constant for $\gamma \geq 6$. For the forested areas, ubRMSE also decreases considerably as γ is increased from 1 to 4, but it continues to decrease as γ is increased further. The difference of optimum (minimum ubRMSE) γ across land cover types could be explained due to the different geophysical processes that drive the changes in the σ' and σ'' and their corresponding time scales. In forest regions, a more pronounced smoothing (corresponding to a higher γ) will not compromise the representation of any short-term dynamics, while a better suppression of noise is achieved. Although the bias in Figure 11(c) does improve for increasing γ, the magnitude of the bias is already very low at low values of γ and the improvement is small compared to those in ubRMSE and correlation. Furthermore, the relation between bias and land cover type is not consistent with the other performance metrics, suggesting that the bias might be a result of artifacts unrelated to the earth's surface, such as the difference in orbit between Metop-A and B.

Violin plots of ubRMSE, bias and correlation for $\hat{\sigma}'_{loc_E}$ and $\hat{\sigma}'_{loc_R}$ are provided in Figure 12. For most land cover types, the performance of $\hat{\sigma}'_{loc_E}$ and $\hat{\sigma}'_{loc_R}$ is very similar in these aggregated statistics. For cropland, shrubland, and herbaceous land

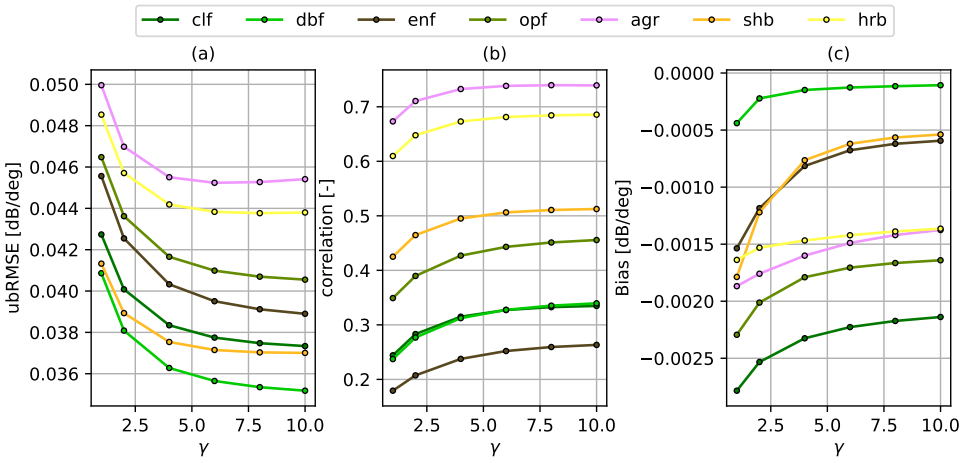

Fig. 11. Mean of ubRMSE (a), Pearson correlation coefficient (b), and bias (c) between σ'_{loc_B} and $\hat{\sigma}'_{loc_R}$ as a function of γ for the subset of 1492 grid points in the study region, sorted by land cover.

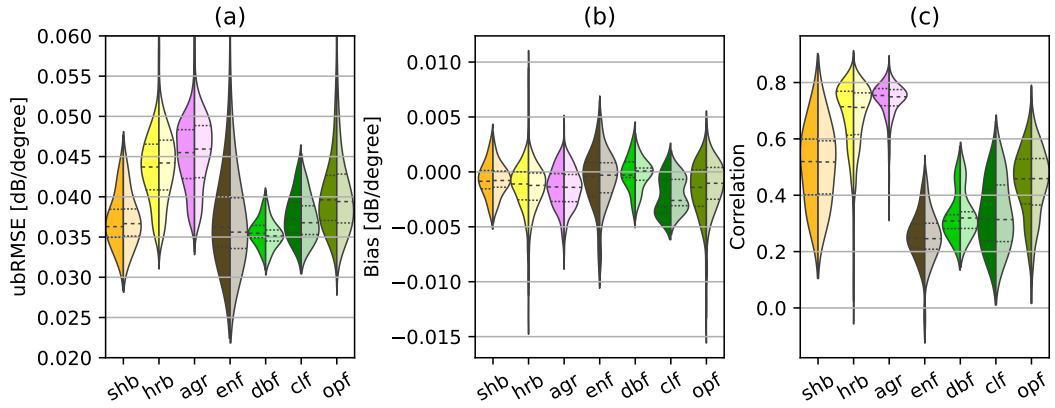

Fig. 12. Violin plot of ubRMSE (left), bias (middle), and Pearson correlation coefficient (right), comparing σ'_{loc_B} to $\hat{\sigma}'_{loc_R}$ (left half of violins), and σ'_{loc_B} to $\hat{\sigma}'_{loc_E}$ (right half of violins) for the 1492 validation points. Results are sorted per land cover class. A gamma of 6 is used for $\hat{\sigma}'_{loc_R}$ and a 21 day *hw* is used for $\hat{\sigma}'_{loc_E}$.

covers, the median ubRMSE of $\hat{\sigma}'_{loc_R}$ is slightly lower than for $\hat{\sigma}'_{loc_E}$, while for the forest types, it is slightly higher. There are no significant differences between $\hat{\sigma}'_{loc_R}$ and $\hat{\sigma}'_{loc_E}$ in bias or correlation for the different land covers. The highest correlations occur for the less vegetated land covers: herbaceous, cropland, and shrubland. This is likely because of the seasonal cycle in vegetation cover in these regions that results in a seasonal cycle in σ'.

Figure 13 shows the ubRMSE and bias for $\hat{\sigma}'_{loc_E}$ and $\hat{\sigma}'_{loc_R}$ computed using σ'_E and σ'_R with various values of half-width and γ, respectively. For $\hat{\sigma}'_{loc_R}$, the bias decreases for increasing γ, whereas no such relation seems to exist for $\hat{\sigma}'_{loc_E}$. A minimum value of the ubRMSE of $\hat{\sigma}'_{loc_R}$ occurs at γ = 8, with γ values of 6 and 10 showing similar performance. For $\hat{\sigma}'_{loc_E}$, the best ubRMSE occurs for a half-width of 21 days. Though the time series of $\hat{\sigma}'_{loc_E}$ look very different, the changes in performance metrics are very subtle between the different half-widths.

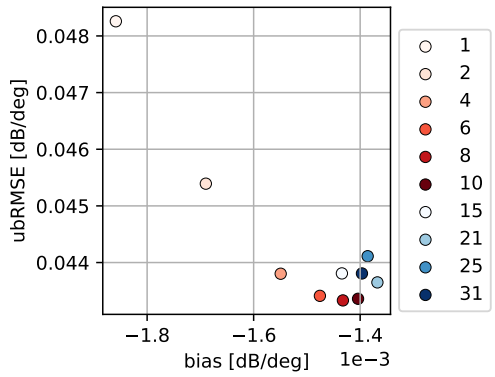

Fig. 13. Average ubRMSE and bias of the 1492 grid points, comparing σ'_{loc_B} to $\hat{\sigma}'_{loc_R}$ (red), and σ'_{loc_B} to $\hat{\sigma}'_{loc_E}$ (blue) with a range of γ and half-width values, respectively.

This is not the case for $\hat{\sigma}'_{loc_R}$, where the time series look alike in terms of timing, but the ubRMSE increases a lot for lower γ, likely due to insufficient suppression of noise. The minimum ubRMSE for $\hat{\sigma}'_{loc_R}$ at γ=8, indicates that around this value an optimum balance between noise suppression and excessive smoothing is achieved. For higher values of γ, the time series will be too smooth, leading to a lower bias, but compromising the ubRMSE. The variation in performance of $\hat{\sigma}'_{loc_R}$ as a function of smoothing conditions seems to follow a pattern with a clear local minimum whereas, for $\hat{\sigma}'_{loc_E}$, changes in smoothing conditions will not yield an evident optimum ubRMSE such as in $\hat{\sigma}'_{loc_R}$.

Figure 14 shows a spatial plot of the error metrics for $\hat{\sigma}'_{loc_E}$ and $\hat{\sigma}'_{loc_R}$, computed for each grid point in the considered region, and interpolated to a finer grid. The highest correlation for both methods occurs in the northwest where vegetation cover is sparser, in line with the results of Figure 12. In Figure 14(c) to (f), a clear pattern of diagonal swaths occurs with a negative bias and increased ubRMSE. The main difference between $\hat{\sigma}'_{loc_E}$ and $\hat{\sigma}'_{loc_R}$ can be seen in the criss-cross pattern of negative bias in Figure 14(c) and (d), which are slightly more negative for $\hat{\sigma}'_{loc_R}$. The spots of high ubRMSE that occur around the Dallas urban area in Figure 14(e) are not present in the ubRMSE of the $\hat{\sigma}'_{loc_R}$ in Figure 14(f). It could be that these spots are caused by the lakes in the vicinity of Dallas, causing outliers in the backscatter and thus σ' as observed by ASCAT. In this case, the impact of these outliers is lower in $\hat{\sigma}'_{loc_R}$ than in $\hat{\sigma}'_{loc_E}$. Overall, spatial patterns in aggregated statistics are similar for both methods.

IV. Discussion

A. Influence of short-term events

The response of the Epanechnikov kernel to a double impulse function as presented in Figure 5(c) shows that superposition of multiple events complicates the interpretation of slope time series by introducing artifacts at a different time than the actual events. For regions where the slope is thought to be influenced by soil moisture or precipitation, high-frequency fluctuations such as those shown in Figure 3 are important [12, 13].

This superposition effect could also be reflected in the results in the real ASCAT time series presented in Figure 6. When looking at the temporal derivative of σ'_R, dips in the slope gradient occur at the time of sharp soil moisture increases in Figure 3, suggesting a similar influence of soil moisture for the simplified time series in Figure 5 and real-time series. Thus, the adverse timing artifacts of slope estimation using the Epanechnikov kernel likely also occur in real time series.

Implications of this superposition are not limited to the timing of slope changes, but also the magnitude of high-frequency variations in slope could be suppressed or amplified. If rapid decreases in slope are superimposed on a signal of interest, these decreases will suppress the σ'_E for the weeks around their occurrence. For example, when using the slope as an indicator for the vegetation water content, such as in [10], not only the timing of the spring peak in slope could vary due to soil moisture dynamics, but also the magnitude of the peak varies because of the presence of soil moisture peaks around the analyzed period, suppressing the slope signal. The convolved nature of slope estimated using the Epanechnikov kernel complicates the identification and isolation of the short term events. Using an estimator that does not use convolution, and thus

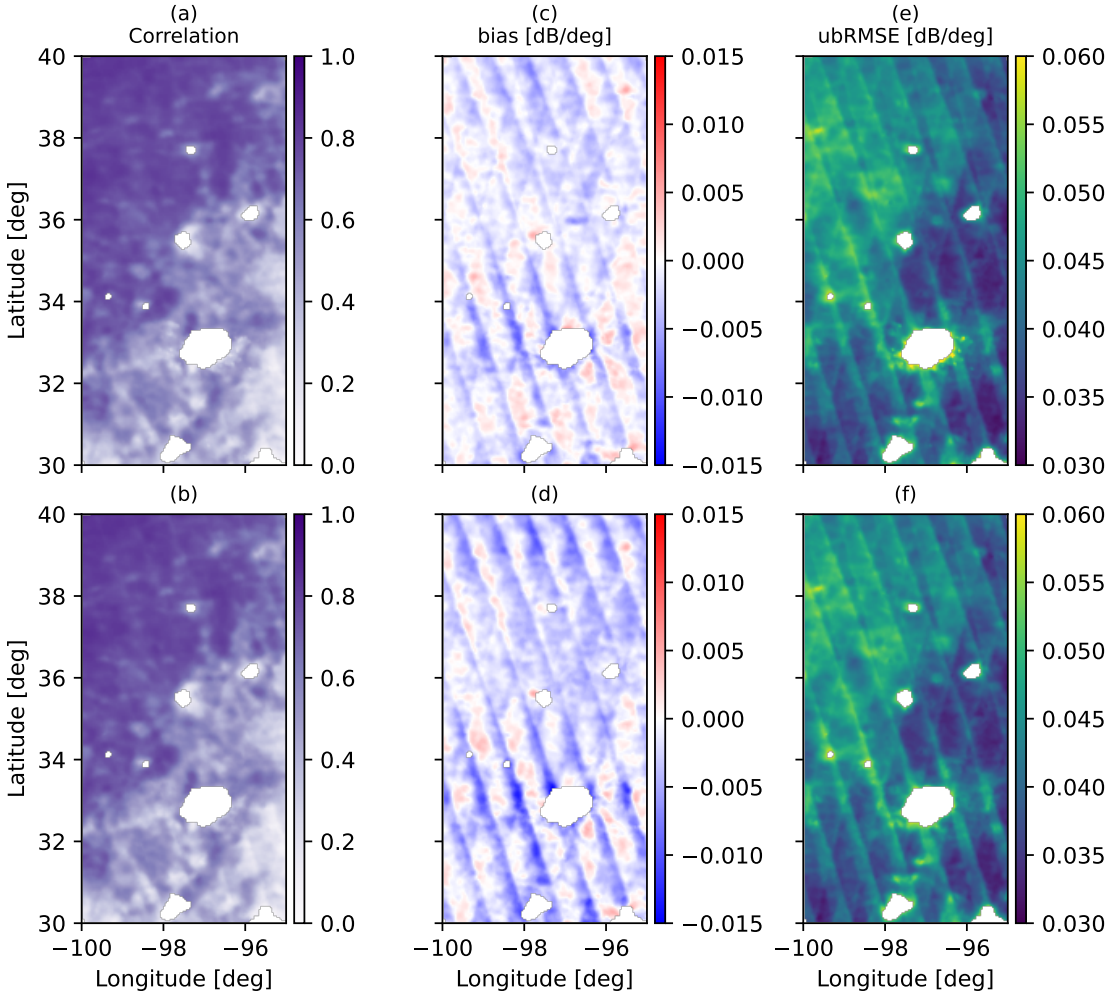

Fig. 14. Pearson correlation coefficient (left), bias (mid) and ubRMSE (right), comparing σ'_{loc_B} to $\hat{\sigma}'_{loc_E}$ with 21-day *hw* (top), and σ'_{loc_B} to $\hat{\sigma}'_{loc_R}$ with γ value of 6 (bottom) in the study area.

better preserves the timing of changes in the input signal could improve the identification of these short-term fluctuations, allowing possible isolation. Steele-Dunne et al. [13] showed that using dynamic estimation of σ' and σ'' using the Epanechnikov method does not enhance soil moisture retrieval from ASCAT compared to using a climatological representation of σ' and σ''. Better results were obtained if the kernel half-width was increased, likely caused by convolved rapid changes in soil and vegetation, which are smoothed out for larger *hw* and in the climatology. This illustrates that the implications of a better representation of these rapid changes in the regularized slope for the retrieval of soil moisture should be investigated in parallel research.

B. Limitations of Metop-B validation

Although it allows us to assess the performance of σ°-θ relation estimations, there are several limita-

tions to using Metop-B local slopes as an observation in validation. Like any type of observation, there is measurement noise in the backscatter observed by ASCAT aboard Metop-B, which is propagated to σ'_{loc}. The magnitude of this noise is not considered in this research, but the presence of this noise limits the minimum ubRMSE and maximum correlation that can be achieved using this validation method. Besides noise, there are differences in orbital geometry and phase, as mentioned in [6], causing a bias between σ' observed by Metop-A and -B, and requiring temporal collocation of the time series. Lastly, since the σ' time series need to be extrapolated to the incidence angles of Metop-B σ'_{loc} using σ'', it is not possible to investigate the errors of σ' and σ'' separately using this method of validation.

C. Configuration of regularization method

The configuration of the regularization method in this research involved a constraint on first differences in the vector of unknown parameters σ' and σ'' of which the strength is driven by scalar γ for σ' and effectively 10 γ for σ''. Various changes to this configuration could be made to improve the performance of this estimation method, such as separate γ parameters for σ' and σ'', additional constraints on second-order differences, or a dynamic γ that would allow temporal or spatial variability on the smoothing constraint [14]. Furthermore, in this research, no information on the uncertainty of individual observations was used in the constrained least squares estimation. The addition of the inverse covariance matrix as a weighing matrix in the constrained least squares computation will mitigate the influence of observations with high uncertainty on the estimated σ' and σ''. In the current setup, the smoothness of the estimated time series is driven by γ, and an appropriate value is determined through cross-validation. There are other methods to compute an appropriate value of γ, such as presented in [22]. As seen in Figure 11, the optimum smoothness varies among land covers, with a clear distinction between regions dominated by sparse vegetation and forested regions. The former regions performing best with a γ between 6 and 8, and the latter performing better for higher values of γ, although the improvement in performance metrics for γ larger than 6 is limited.

As seen in Figure 3, the magnitude of short-term fluctuations increases for decreasing gamma, so for higher values of gamma, short-term fluctuations are dampened more. Since these short-term fluctuations may contain valuable information, and performance does not improve significantly for $\gamma > 6$ for most land covers, it is recommended that a γ of 6 is used to constrain the first differences in σ' and σ'' estimated using the regularization method. While there could be some benefit to optimizing γ per land cover, this would also introduce a need for auxiliary data and could introduce artifacts related to the land cover data. Looking beyond the use of this method for estimating historical data sets of ASCAT slope, it is interesting to consider the consequences of implementing the proposed method for the estimation of slope in a near real-time context. Though this is not investigated in this study, it is expected that the memory of the first difference constraint is limited to a few weeks with the recommended value of γ. This limited memory allows new σ' and σ'' values to be added to an existing time series as new observations become available, while requiring only a few weeks of ASCAT data for the estimation rather than the entire dataset. Thus, large computational costs for extending records of σ' and σ'' estimates can likely be avoided and could be of similar scale as for the kernel smoothing approach.

V. CONCLUSIONS

This study demonstrates that ASCAT σ°-θ relation can be estimated without the use of a smoothing kernel, as used in the current method for estimating the σ°-θ relation. A disadvantage of the current smoothing kernel is the relatively uniform weighing of observations from multiple weeks contributing to the estimation of the σ°-θ relation for a single day, with relatively high weights assigned to observations near the bounds of the kernel, 21 days from the day of interest, following the Epanechnikov kernel. Day-to-day changes in the σ°-θ relation estimated using this method are driven by the exclusion and inclusion of past and future observations at the bounds of the Epanechnikov kernel. This results

in a discrepancy between the timing of short-term changes in the observations and short-term changes in estimated σ' and σ'' time series. Using a method for constrained least squares, σ' and σ'' time series can be estimated with a penalty for the sum of squared day-to-day differences of σ' and σ''. This regularization method does not include a smoothing kernel, and estimates of σ' and σ'' are mainly influenced by observations within a few days around the date of interest, allowing better conservation of the timing of events throughout the estimation of the σ°-θ relation. The difference between the two methods is mainly visible in the short-term fluctuations in the time series of σ', where both timing and magnitudes are influenced by the half-width of the smoothing kernel. In contrast, for the regularization method, only the magnitude of these fluctuations changes under different smoothing conditions.

The validation in terms of reproducing the Metop-B ${\sigma'}_{loc}$ using Metop-A σ' and σ'' showed that when averaged in time and over many grid points, the σ'_E and σ'_R yield very similar performance. Most performance metrics do not vary significantly between the two approaches. The main improvement is a decrease in ubRMSE for land covers with sparse vegetation.

The main difference between the smoothing kernel and regularization approach is that the timing of events is better represented in σ'_R than in σ'_E. This benefit is not clear in the aggregated statistics but becomes clear in an analysis of individual time series. The conservation of this timing is essential for the identification of the various geophysical processes driving changes in σ', such as VWC, vegetation structure, and soil moisture content. The ability to disentangle these processes could allow us to isolate slope changes related to vegetation-related processes from other geophysical processes, paving the way for a vegetation-oriented data product based on ASCAT slope. Additionally, the consistency of σ' with different data sets such as in-situ soil moisture measurements, land surface models, or other satellite observations will benefit from the improved temporal representation of changes.

There are several options in the implementation of the regularization method that could be investigated to further improve the estimation of σ' and σ''. In the configuration used in this study, in which a constraint is applied to the first differences of σ' and σ'', it is recommended that a γ of 6 is used to mitigate the amplification of observation noise in the estimated time series, while avoiding unnecessary smoothing of real short term dynamics. Alternative constraints, weighing of observations, or a dynamic application of constraints could further improve the representation of the backscatter-incidence angle relationship and hence the σ' and σ'' time series estimated from ASCAT observations. Finally, it is expected that implementation of this method in near real-time estimation should not lead to inflated computational effort compared to the kernel smoothing approach.

Future research should investigate the impact of this new approach to estimate the σ°-θ relation on its potential to improve our ability to study vegetation water dynamics using ASCAT. Pre-processing steps including outlier removal will also need to be revisited to account for the increased sensitivity of the estimated slope to individual observations when this approach is implemented globally. Lastly, the computational cost of the regularization method should be investigated before regularized slope is computed at a global scale.

APPENDIX

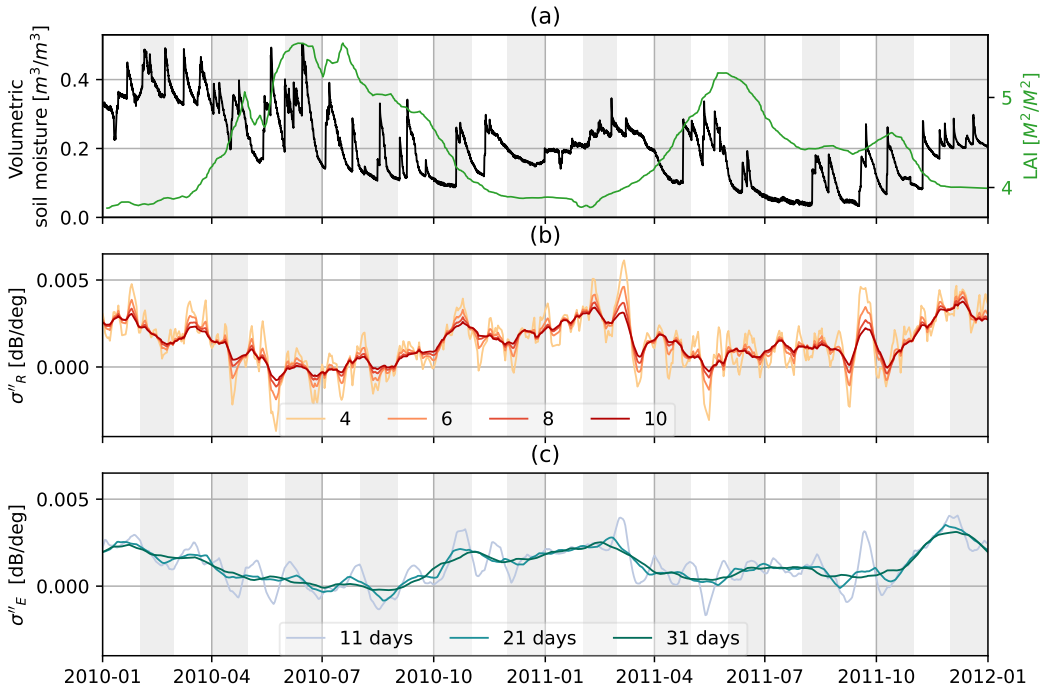

Fig. 15. Two years of ASCAT curvature time series near Stillwater, Oklahoma, USA. The top panel (a) shows in-situ soil moisture observations from the Stillwater-5-WNW station[18] and leaf area index (LAI) from MODIS[20]. The middle panel (b) shows σ''_R with γ values of 4, 6, 8, and 10. (c) shows σ''_E with kernel half widths of 11, 21, and 31 days.

ACKNOWLEDGMENT

This publication has been prepared using European Union's Copernicus Land Monitoring Service information.

REFERENCES

[1] Z. Bartalis, W. Wagner, V. Naeimi, S. Hasenauer, K. Scipal, H. Bonekamp, J. Figa, and C. Anderson, "Initial soil moisture retrievals from the METOP-A Advanced Scatterometer (ASCAT)," *Geophysical Research Letters*, vol. 34, no. 20, 2007. [Online]. Available: https://onlinelibrary.wiley.com/doi/abs/10.1029/2007GL031088

[2] W. Wagner, G. Lemoine, and H. Rott, "A Method for Estimating Soil Moisture from ERS Scatterometer and Soil Data," *Remote Sensing of Environment*, vol. 70, no. 2, pp. 191–207, Nov. 1999. [Online]. Available: https://www.sciencedirect.com/science/article/pii/S003442579900036X

[3] V. Naeimi, K. Scipal, Z. Bartalis, S. Hasenauer, and W. Wagner, "An Improved Soil Moisture Retrieval Algorithm for ERS and METOP Scatterometer Observations," *IEEE Transactions on Geoscience and Remote Sensing*, vol. 47, no. 7, pp. 1999–2013, Jul. 2009, conference Name: IEEE Transactions on Geoscience and Remote Sensing.

[4] T. Melzer, "Vegetation Modelling in WARP

6.0," in *Proceedings of the EUMETSAT Meteorological Satellite Conference,*, Vienna, Austria, Sep. 2013, pp. 16–20.

[5] W. Wagner, G. Lemoine, M. Borgeaud, and H. Rott, "A study of vegetation cover effects on ERS scatterometer data," *IEEE Transactions on Geoscience and Remote Sensing*, vol. 37, no. 2, pp. 938–948, Mar. 1999, conference Name: IEEE Transactions on Geoscience and Remote Sensing. [Online]. Available: https://ieeexplore.ieee.org/document/752212

[6] S. Hahn, C. Reimer, M. Vreugdenhil, T. Melzer, and W. Wagner, "Dynamic Characterization of the Incidence Angle Dependence of Backscatter Using Metop ASCAT," *IEEE Journal of Selected Topics in Applied Earth Observations and Remote Sensing*, vol. 10, no. 5, pp. 2348–2359, May 2017, conference Name: IEEE Journal of Selected Topics in Applied Earth Observations and Remote Sensing.

[7] M. Vreugdenhil, S. Hahn, T. Melzer, B. Bauer-Marschallinger, C. Reimer, W. A. Dorigo, and W. Wagner, "Assessing Vegetation Dynamics Over Mainland Australia With Metop ASCAT," *IEEE Journal of Selected Topics in Applied Earth Observations and Remote Sensing*, vol. 10, no. 5, pp. 2240–2248, May 2017, conference Name: IEEE Journal of Selected Topics in Applied Earth Observations and Remote Sensing. [Online]. Available: https://ieeexplore.ieee.org/abstract/document/7762756

[8] S. C. Steele-Dunne, S. Hahn, W. Wagner, and M. Vreugdenhil, "Investigating vegetation water dynamics and drought using Metop ASCAT over the North American Grasslands," *Remote Sensing of Environment*, vol. 224, pp. 219–235, Apr. 2019. [Online]. Available: https://linkinghub.elsevier.com/retrieve/pii/S0034425719300045

[9] A. Petchiappan, S. C. Steele-Dunne, M. Vreugdenhil, S. Hahn, W. Wagner, and R. Oliveira, "The influence of vegetation water dynamics on the ASCAT backscatter–incidence angle relationship in the Amazon," *Hydrology and Earth System Sciences*, vol. 26, no. 11, pp. 2997–3019, Jun. 2022. [Online]. Available: https://hess.copernicus.org/articles/26/2997/2022/

[10] I. Pfeil, W. Wagner, M. Forkel, W. Dorigo, and M. Vreugdenhil, "Does ASCAT observe the spring reactivation in temperate deciduous broadleaf forests?" *Remote Sensing of Environment*, vol. 250, p. 112042, Dec. 2020. [Online]. Available: https://www.sciencedirect.com/science/article/pii/S0034425720304120

[11] X. Shan, S. Steele-Dunne, M. Huber, S. Hahn, W. Wagner, B. Bonan, C. Albergel, J.-C. Calvet, O. Ku, and S. Georgievska, "Towards constraining soil and vegetation dynamics in land surface models: Modeling ASCAT backscatter incidence-angle dependence with a Deep Neural Network," *Remote Sensing of Environment*, vol. 279, p. 113116, Sep. 2022. [Online]. Available: https://www.sciencedirect.com/science/article/pii/S0034425722002309

[12] I. Greimeister-Pfeil, W. Wagner, R. Quast, S. Hahn, S. Steele-Dunne, and M. Vreugdenhil, "Analysis of short-term soil moisture effects on the ASCAT backscatter-incidence angle dependence," *Science of Remote Sensing*, vol. 5, p. 100053, Jun. 2022. [Online]. Available: https://www.sciencedirect.com/science/article/pii/S2666017222000153

[13] S. C. Steele-Dunne, S. Hahn, W. Wagner, and M. Vreugdenhil, "Towards Including Dynamic Vegetation Parameters in the EUMETSAT H SAF ASCAT Soil Moisture Products," *Remote Sensing*, vol. 13, no. 8, p. 1463, Jan. 2021, number: 8 Publisher: Multidisciplinary Digital Publishing Institute. [Online]. Available: https://www.mdpi.com/2072-4292/13/8/1463

[14] T. Quaife and L. Philip, "Temporal Constraints on Linear BRDF Model Parameters," *IEEE TRANSACTIONS ON GEOSCIENCE AND REMOTE SENSING*, vol. 48, May 2010.

[15] S. Twomey, *Introduction to the Mathematics of Inversion in Remote Sensing and Indirect*

Measurements, Feb. 1977. [Online]. Available: https://shop.elsevier.com/books/introduction-to-the-mathematics-of-inversion-in-remote-sensing-and-indirect-measurements/twomey/978-0-444-41547-9

[16] S. Hahn, "TUW-GEO/fibgrid: v0.0.6," Nov. 2024. [Online]. Available: https://doi.org/10.5281/zenodo.14187002

[17] E. C. D.-G. J. R. Centre, "Land cover 2015-2019 (raster 100 m), global, annual," https://land.copernicus.eu/en/products/global-dynamic-land-cover/copernicus-global-land-service-land-cover-100m-collection-3-epoch-2019-globe, 2019-05-14.

[18] J. E. Bell, M. A. Palecki, C. B. Baker, W. G. Collins, J. H. Lawrimore, R. D. Leeper, M. E. Hall, J. Kochendorfer, T. P. Meyers, T. Wilson, and H. J. Diamond, "U.S. Climate Reference Network Soil Moisture and Temperature Observations," *Journal of Hydrometeorology*, vol. 14, no. 3, pp. 977–988, Jun. 2013, publisher: American Meteorological Society Section: Journal of Hydrometeorology. [Online]. Available: https://journals.ametsoc.org/view/journals/hydr/14/3/jhm-d-12-0146_1.xml

[19] W. Dorigo, P. van Oevelen, W. Wagner, M. Drusch, S. Mecklenburg, A. Robock, and T. Jackson, "A New International Network for in Situ Soil Moisture Data," *Eos, Transactions American Geophysical Union*, vol. 92, no. 17, pp. 141–142, 2011. [Online]. Available: https://onlinelibrary.wiley.com/doi/abs/10.1029/2011EO170001

[20] R. Myneni, Y. Knyazikhin, and T. Park, "MODIS/Terra Leaf Area Index/FPAR 8-Day L4 Global 500m SIN Grid V061," 2021. [Online]. Available: https://lpdaac.usgs.gov/products/mod15a2hv061/

[21] A. Gruber, G. De Lannoy, C. Albergel, A. Al-Yaari, L. Brocca, J. C. Calvet, A. Colliander, M. Cosh, W. Crow, W. Dorigo, C. Draper, M. Hirschi, Y. Kerr, A. Konings, W. Lahoz, K. McColl, C. Montzka, J. Muñoz-Sabater, J. Peng, R. Reichle, P. Richaume, C. Rüdiger, T. Scanlon, R. van der Schalie, J. P. Wigneron, and W. Wagner, "Validation practices for satellite soil moisture retrievals: What are (the) errors?" *Remote Sensing of Environment*, vol. 244, p. 111806, Jul. 2020. [Online]. Available: https://www.sciencedirect.com/science/article/pii/S0034425720301760

[22] J. Zobitz, T. Quaife, and N. K. Nichols, "Efficient hyper-parameter determination for regularised linear brdf parameter retrieval," *International Journal of Remote Sensing*, vol. 41, no. 4, pp. 1437–1457, 2020.

Paco Frantzen was born in Amsterdam, The Netherlands, in 1997. He obtained his BSc. degree in Aerospace Engineering in 2020, and MSc. in Civil Engineering in 2022 at the Delft University of Technology, Delft, The Netherlands. During his studies, in 2021 he was an Intern at the Netherlands Aerospace Center in Amsterdam, The Netherlands, and in 2022 was a Visiting Scientist at the Remote Sensing & Topographic LiDAR Research Group of Universität Innsbruck in Innsbruck, Austria. Currently he is a PhD candidate at Delft University of Technology at the department of Geoscience and Remote Sensing.

Susan C. Steele-Dunne received the S.M. and Ph.D. degrees in hydrology from the Massachusetts Insti- tute of Technology, Cambridge, MA, USA, in 2002 and 2006, respectively. She has been with the Fac- ulty of Civil Engineering and Geosciences at Delft University of Technology, in the Netherlands since 2008. Prof. Steele-Dunne leads the M-WAVE group, who perform research from field to global scales, combining in-situ and spaceborne sensors to improve our understanding of microwave interactions with vegetation. Her research interests include the the use of data assimilation, modeling and machine learning to exploit spaceborne radar instruments for applications in ecosystem and agricultural monitoring.

Tristan Quaife received the B.Sc. degree in environmental chemistry from the University of Hertfordshire, Hatfield, UK, in 1997 and the Ph.D. degree in remote sensing from the University of Wales, Swansea, UK, in 2001.

He is currently Professor of Earth System Science with the University of Reading in the UK and the UK National Centre for Earth Observation. Previously, he was a lecturer in Geography at the University of Exeter, and held postdoctoral positions with University College London, London, UK, originally in the Center for Terrestrial Carbon Dynamics and then the National Center for Earth Observation. His primary research interests are radiative transfer in plant canopies and data assimilation techniques to interface land surface models with Earth observation data.

Mariette Vreugdenhil received the B.Sc. and M.Sc. degree in earth sciences with an emphasis on re- mote sensing from Vrije Universiteit Amsterdam, Amsterdam, The Netherlands, in 2009 and 2011, respectively. She obtained a Ph.D. in remote sensing with the Centre for Water Resource Systems and Department of Geodesy and Geoinformation, TU Wien, Vienna, Austria in 2016. Currently, she works as a senior scientist at the Department of Geodesy and Geoinformation at TU Wien. Her research inter- ests are the development of retrieval algorithms for vegetation and soil moisture from active microwave observations, in particular from the Advanced SCATterometer on-board of EUMETSAT Metop satellites and from the Synthetic Aperture Radars on-board of the Copernicus Sentinel-1 satellites.

Sebastian Hahn Sebastian Hahn received the B.Sc. degree in geodesy and geoinformatic engineering and the M.Sc. degree in geodesy and geophysics from the Vienna University of Technology (TU Wien), in 2009 and 2011, respectively. He is currently pursuing his Ph.D. degree in microwave remote sensing at TU Wien. He joined the Department of Geodesy and Geoinformation at TU Wien (Vienna, Austria) in 2009, where he currently serves as a Senior Scientist. His research focuses on remote sensing of land surfaces using active microwave instruments, developing soil moisture retrieval algorithms, and advancing software engineering for remote sensing data services.

Wolfgang Wagner (Senior Member, IEEE) received the Dipl.-Ing. degree in physics and the Dr.techn. degree in remote sensing from TU Wien, Vienna, Austria, in 1995 and 1999, respectively. From 1999 to 2001, he was with DLR, Oberpfaffenhofen, Germany. In 2001, he was appointed as a Professor for remote sensing at TU Wien. He is a Co-Founder of the Earth Observation Data Centre (EODC), Vienna. He has developed models for retrieving soil moisture and other land surface variables from scatterometer, synthetic aperture radar (SAR), and full-waveform LiDAR observations. His main research interests are to gain a physical understanding of the mechanisms driving the interaction of electromagnetic waves with the land surface. Dr. Wagner is a member of the advisory groups for METOP-SG SCA, Sentinel-1 NG, and HydroGNSS. In support of his master's and Ph.D. studies, he won fellowships to carry out research at NASA, ESA, and the EC Joint Research Centre. He was a recipient of the ISPRS Frederick J. Doyle Award and the Friedrich Hopfner Medal awarded by the Austrian Geodetic Commission. From 2008 to 2012, he served as the ISPRS Commission VII President; from 2009 to 2011, he served as an Editor-in-Chief of the open access journal "Remote Sensing,"; and from 2016 to 2019, he served as the Chair for the GCOS/WCRP Terrestrial Observation Panel for Climate.